Micropillared Surface to Enhance the Sensitivity of a Love-Wave Sensor

Jérémy Bonhomme,[1,2,3,†] Mourad Oudich,[1,4,*] Mohamed Lamine Fayçal Bellaredj,[1] Jean-François Bryche,[2,3] Pedro Alberto Segura Chavez,[1,2,3] Denis Beyssen,[1] Paul G. Charette,[2,3,‡] and Frédéric Sarry[1,§]

[1] *Université de Lorraine, CNRS, Institut Jean Lamour, F-54000 Nancy, France*

[2] *Laboratoire Nanotechnologies Nanosystèmes (LN2)-CNRS IRL-3463, Université de Sherbrooke, Sherbrooke, Québec J1K 2R1, Canada*

[3] *Institut interdisciplinaire d'innovation technologique (3IT), 3000 boulevard de l'Université, J1K 0A5 Sherbrooke, Québec, Canada*

[4] *Graduate Program in Acoustics, The Pennsylvania State University, University Park, Pennsylvania, 16802, USA*

(Received 9 December 2021; revised 28 March 2022; accepted 22 April 2022; published 13 June 2022)

Surface-acoustic-wave (SAW) sensors have undergone outstanding developments during the last decades. However, for biosensing applications, they struggle to compete with optical sensing technologies. In this work, we present a Love-wave-based sensing platform that leverages the use of the local resonances of micropillars fabricated on the surface of the guiding layer. We demonstrate numerically and experimentally that the Love-wave interaction with the micropillars produces sharp attenuation dips in the transmission spectrum. These dips are associated with the excitations of flexural and torsional resonance modes of the pillars. We utilize these modes to achieve higher detection sensitivity of temperature variation and mass loading using sugar and microbeads concentrations in aqueous solutions. Integrating a lattice of micropillars into SAW-based devices offers a strong potential for detecting low particles concentrations.

DOI: 10.1103/PhysRevApplied.17.064024

I. INTRODUCTION

The last decade has witnessed the rapid development of sensors and biosensors for a large set of applications, encompassing food processing, medical diagnosis, biosensing, and military defense [1,2]. Particularly, surface-acoustic-wave- (SAW) based microsensors have attracted great attention as they are known to be cost-effective with a remarkable capability for the real-time monitoring of cells and biological molecules [3]. Rapid advances in microfabrication and characterization have enabled the efficient use of SAW sensors, as they can be miniaturized and embedded into lab-on-a-chip, which extends the functionalities of SAWs beyond sensing to cell manipulations using acoustic tweezers, fluid steering, and mixing [4–9]. In the case of biosensing, a particular type of SAW is utilized, known as Love waves, which are guided surface elastic waves along a finite-thickness material layer deposited on the surface of a substrate. Love waves can exist only if the velocity of the shear bulk wave of the layer is lower than that of the substrate. Contrary to Rayleigh waves, which are polarized along the sagittal plane, Love waves have a shear horizontal polarization with no displacement along the direction perpendicular to the surface. This characteristic makes Love waves more suitable for chemical and biological sensing in liquid and viscous environments in contact with the surface, as they can travel with low attenuation and have weak acoustic energy radiation into liquid environments [10–13]. In general, a Love-wave microsensor is fabricated using a polymer layer, such as SU-8, on a piezoelectric substrate, like quartz, lithium niobate ($LiNbO_3$), or tantalate ($LiTaO_3$), with interdigital transducers to generate and detect the wave signals using direct and inverse piezoelectric effects. A biosensing thin layer is deposited on the surface so that any adsorption of biomolecules induces changes in the mass and viscosity of the biosensing layer, hence leading to a shift in the phase velocity and/or amplitude of the wave [3]. Despite efforts to increase the sensing performance of SAW devices, they have reached their limit in terms of sensitivity, as they struggle to compete with recent optical technologies that are based on plasmonic metamaterials [14–16] and optomechanics [17–19], which enable single-molecule and nanoparticle detection.

Meanwhile, the last three decades have seen the emergence and development of phononic crystals and elastic metamaterials that serve as fertile platforms for exotic wave phenomena and precise acoustic and elastic waves control, for filtering, waveguiding, acoustic

*mourad.oudich@univ-lorraine.fr
†jeremy.bonhomme@insp.jussieu.fr
‡Paul.G.Charette@usherbrooke.ca
§frédéric.sarry@univ-lorraine.fr

superfocusing, and enhanced sensing [20–40]. Multiple studies have demonstrated the potential of phononic crystals for sensing, such as propanol-concentration detection [28,35,36], liquid-type determination [37], ethanol-concentration-variation sensing [26,38], detection of the molar ratio of 1-methyl-3-octylimidazolium chloride in methanol [39], and photoacoustic mass sensing at 100 GHz [40]. Thus, it is of great interest to integrate acoustic metamaterials into SAW-based platforms through the structural design of the surface to increase their sensing performance. In fact, studies have demonstrated that SAWs can interact with a periodic lattice of pillar-shaped resonators decorating the surface of a substrate, and the interaction excites individual localized natural resonances of each pillar. These resonances lead to strong attenuation of SAWs in the spectrum at wavelengths larger than the pillars dimensions and the periodicity of the lattice [29–31,41–44]. The advantage of such a system is that the coupling between SAWs and the resonators occurs below the sound line, which renders the phenomenon confined within the surface with rapid evanescent decay of the wave field into the bulk substrate. Khelif *et al*. [31] investigated Rayleigh-wave dispersion by a square lattice of pillars decorating the surface of a silicon substrate, and demonstrated the opening of band gaps created from the SAW interaction with the resonance modes of the pillars. At the microscale, Robillard *et al.* [41] presented an experimental observation of individual resonances of cubic metal pillars decorating the surface of a substrate. Achaoui *et al.* [42] used an optical measurement technique to characterize the vibrational motion of individual pillars at resonance and observed SAW attenuation by a square lattice of cylindrical nickel pillars deposited on a lithium niobate substrate. Yudistira *et al.* [43] explored SAW dispersion by a lattice of micropillars and showed theoretically and experimentally both the Bragg- and local-resonance-based band gaps. SAW attenuation by the resonance of the pillars was also demonstrated experimentally using a lattice of metallic nanodisks [45] and pillars in holes [46]. Pillars can also be used to confine and store the mechanical-strain energy carried by SAWs [29]. Recently, Raguin *et al*. [34] used SAW interactions with two coupled resonant pillars to manipulate the elastic energy distribution on the substrate surface. These designs are of great interest for potential applications in biosensing, especially if the resonance modes are well tailored for this purpose. We recently proposed the design of a phononic micropillar lattice decorating the surface of a substrate, where each micropillar displayed resonance modes with highly-confined-strain energy density [32,33,47]. These resonances can be excited by Love waves and are depicted in the transmission spectra as sharp resonance decays (dips) with high quality factors. We theoretically and numerically demonstrated that this kind of SAW-based metamaterial design had great potential for increasing the sensitivity toward small amounts of nanoparticles [33]. Following this hypothesis, we build an experimental Love-wave-based platform that exploits micropillar resonances to enhance the sensing performance. The device is composed of two interdigital transducers for the excitation and detection of the Love waves, with a guiding layer and micropillars made of a polymeric photoresist. The interaction between Love waves and the pillars is characterized both numerically and experimentally. We then investigate the evolution of the resonance frequency of the pillars as a function of temperature to validate our experimental protocols and verify the limits of the utilization of the system. Finally, we conduct three different experimental sensing tests: water-droplet volume detection, sugar concentration in water, and polystyrene microbeads concentration in solution.

II. MICROPILLARS-BASED LOVE-WAVE SENSOR

Our system is a Love-wave-based platform made of an epoxy (SU-8) guiding layer on top of a lithium niobate Y+36° cut ($LiNbO_3$ Y+36°) piezoelectric substrate (Love-wave velocity of 3990 m/s). The guiding layer is deposited on top of the interdigitated electrodes (IDTs) and used for the excitation and detection of Love waves. The spacing between successive IDT fingers is 70 μm, which leads to an operating frequency of 35 MHz. A hardbaking process is applied to the SU-8 guiding layer by heating up the device to 150 °C for 20 min. A square lattice of cylindrical micropillars is fabricated on top of the guiding layer between the IDTs in the propagating path of the Love wave. The pillars are made of SU-8 photoresist material, the same as the guiding layer. A schematic representation of the device is presented in Fig. 1(a). The SU-8 pillars can also be hardbaked through the same process as the guiding layer.

To gain insights into the interaction of Love waves with a micropillar, numerical simulations are carried out using the commercial software COMSOL Multiphysics. We first determine the resonance frequencies of a single SU-8 micropillar by performing an eigenfrequency study. For this, it is essential to characterize the elastic parameters and geometry of the micropillar, as it is expected that hardbaking will not only affect its stiffness but also its geometrical size. We characterize the Young's modulus of the SU-8 photoresist using nanoindentation [48–50]. The tests present a Young's modulus of 5.12 GPa for nonhardbaked SU-8, while this value rises to 5.56 GPa after hardbaking. We fabricate pillars with a mean diameter of 4 μm and a height of 4.5 μm before hardbaking. After hardbaking, the pillars' mean diameter and height are reduced to 3.5 and 4 μm, respectively, which corresponds to a reduction of almost 32% of their volume. The eigenfrequency simulation shows that, below 80 MHz, the pillars essentially have two kinds of resonance modes: a flexural and a

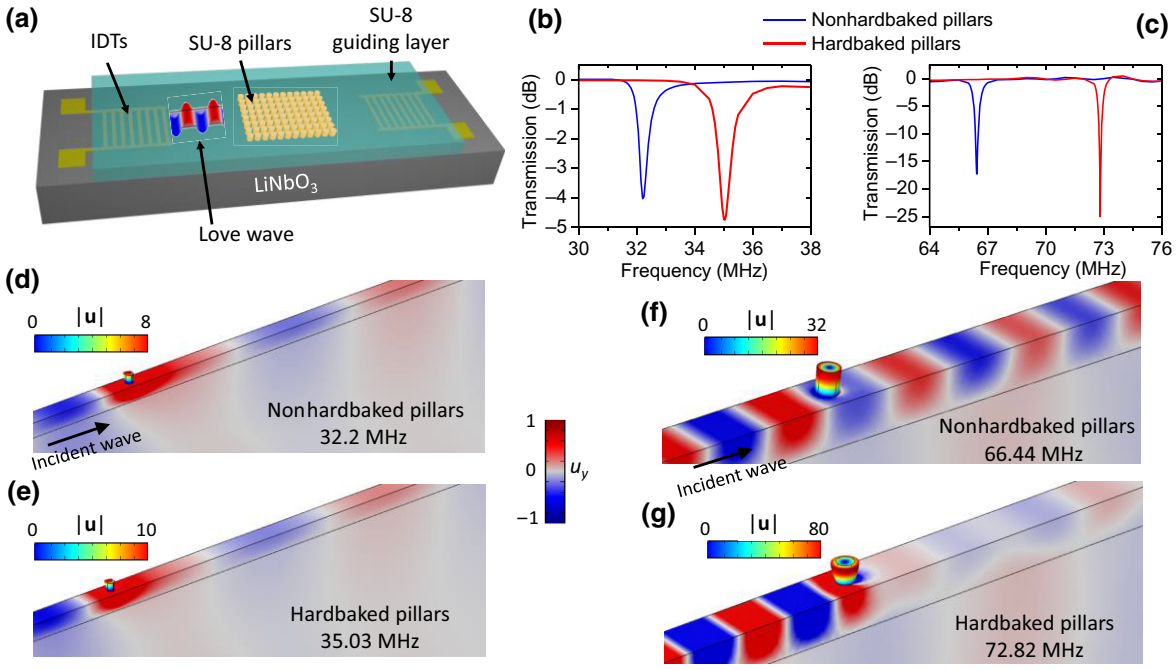

FIG. 1. (a) Schematic view of the complete device. Computed Love-wave transmission spectrum for nonhardbaked (blue curves) and hardbaked (red curves) SU-8 pillars around the resonance frequencies of flexural mode (b) and torsional mode (c). Displacement field amplitudes for nonhardbaked [(d), (f)] and hardbaked SU-8 pillars [(e), (g)] for flexural [(d), (e)] and torsional mode [(f), (g)].

tortional vibration located at 32.2 and 66.4 MHz, respectively, for the case of nonhardbaked pillars, while these modes shift to 34.4 and 73.4 MHz, respectively, for the hardbaked pillars. To be able to observe the tortional-mode resonance with our device, we can either modify the operating frequency of the IDTs or change the dimensions of the pillars. For instance, the height of the pillars must be increased to 10 μm to lower the torsional-mode resonance frequency at 35 MHz.

To study the Love-wave interaction with the pillars, we conduct transmission simulations in the frequency domain by using COMSOL with the same modeling process as that described in our previous work [33]. Figures 1(b) and 1(c) present the results of the transmission spectra for the two cases of hardbaked and nonhardbaked pillars around the frequencies of the flexural and tortional resonance modes. For the nonhardbaked pillar, the transmission spectra shows an attenuation of the Love wave with a dip at 32.2 MHz, corresponding to an excitation of the flexural mode, with an attenuation of 4 dB and a quality factor of 82 [blue curve in Fig. 1(b)]. The torsional mode creates a dip at 66.44 MHz with an attenuation of 17 dB and a higher quality factor of 229 [blue curve in Fig. 1(c)]. In the case of the hardbaked pillars, we observe a shift of the attenuation dips toward higher frequencies. The flexural mode's resonance frequency is located at 35.03 MHz, while that of the torsional mode is at 72.82 MHz [red curves in Figs. 1(b) and 1(c), respectively]. In addition, the attenuations of the Love waves for the two resonance modes of the hardbaked pillars are higher than the attenuations produced by the nonhardbaked pillars. For the flexural mode, the attenuation is slightly increased to 4.75 dB and the quality factor reaches 90, while the attenuation is increased to 25 dB for the torsional mode, and the quality factor is estimated to be 809.

Figures 1(d)–1(g) present the wave fields of each case of the resonance modes for the hardbaked and nonhardbaked pillars. As we are dealing with Love-wave propagation, we represent the transverse-displacement field in the substrate (u_y), while we plot the total displacement field $\|\mathbf{u}\| = (|u_x|^2 + |u_y|^2 + |u_z|^2)^{1/2}$ in the pillar at the resonance frequencies. The maximum displacement field on the pillar is located on the very top of the structure for the two modes. In all four subfigures Figs. 1(d)–1(g), we can clearly observe that the transmitted wave is attenuated at the resonances. The attenuation is barely distinguishable for the case of flexural modes between the hardbaked and nonhardbaked cases when looking at the displacement fields [Figs. 1(d) and 1(e)], while we can see that, for the case of the torsional mode, the wave is strongly attenuated when the pillar is hardbaked [Figs. 1(f) and 1(g)]. Furthermore, for the case of the hardbaked pillars, we can clearly observe that the maximum of the displacement-field amplitude in the pillar is 10 times higher than the amplitude of the Love wave for the flexural mode [Fig. 1(e)]. In contrast, this amplitude ratio reaches 80 for the case of the torsional mode [Fig. 1(g)].

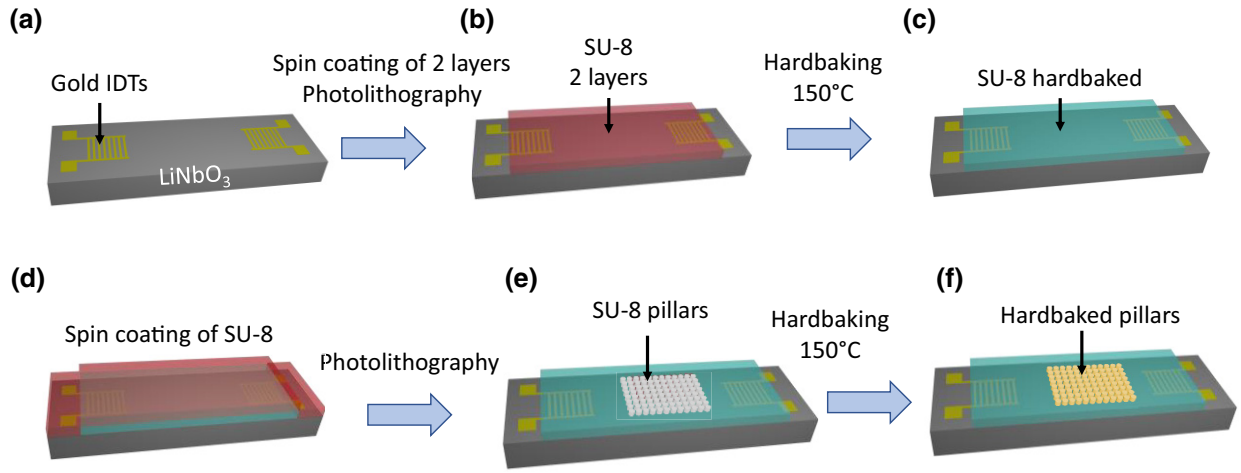

FIG. 2. (a) Deposition of gold IDTs on a $LiNbO_3$ substrate. (b) Spin-coating deposition of SU-8 photoresist (10 μm thickness) where the electrical contacts are liberated by a photolithography process. (c) SU-8 resist is hardbaked by heating the substrate to 150 °C for 20 min. (d) Spin-coating deposition of SU-8 photoresist (5 μm). (e) Photolithography process to obtain a lattice of pillars between the IDTs. (f) Pillars are hardbaked by heating the device to 150 °C for 20 min.

We also calculate the elastic band structure for the case of a square lattice of pillars on the surface of the SU8 guiding layer on $LiNbO_3$, where the coupling between the resonant modes and the Love wave is depicted in Appendix A.

III. SAMPLE FABRICATION AND EXPERIMENTAL CHARACTERIZATION

To generate the Love wave, we use a $LiNbO_3$ Y+36° substrate on which the IDTs, guiding layer, and pillars array are deposited. For IDTs deposition, we use spin-coated AZ 5214 E reversal photoresist (product by Merck) at 3000 rpm to obtain a 1.6-μm-thick layer of resist. Then we expose the substrate to a dose of 55 mJ/cm^2 with a MJB4 mask aligner (SUSS MicroTech) and chemically developed it to pattern the IDTs at 144-μm wavelength. Then we evaporate a bonding layer of 10 nm of titanium and 150 nm of gold. Finally, we remove the photoresist using Remover 1165 (Microposit) to release the electrodes. Regarding the guiding layer, we spin-coat two successive layers of SU-8 2005 photoresist over the IDTs at a speed of 2500 rpm to obtain a final layer of 10 μm thick after exposure (130 mJ/cm^2) and development. The mask used in this step allows us to release the electrical contacts from the SU-8. Then we hardbake the SU-8 layer at 150 °C for 20 min. This step increases the rigidity of the polymer and makes it more resistant to solvents. However, it reduces the thickness of the guiding layer by around 11%. The final step is to build the pillars on top of the guiding layer. We use a direct photolithography process on the SU-8 photoresist. We spin-coat a layer of SU-8 2005 with the same parameters as the deposition of the guiding layer, and we expose it to obtain a matrix of pillars (100 mJ/cm^2). The obtained pillars are 4.5 μm high and 4 μm in diameter with a periodicity of 9 μm. The hardbaking step is performed by heating the devices at 150 °C for 20 min, which reduces the height and diameter of the pillars to 4 and 3.5 μm, respectively. The fabrication steps are summarized in Fig. 2. Figure 3(a) presents the fabricated device and scanning-electron-microscope images of the lattice of pillars.

For the electrical characterization of the device, we connect the samples to a probe station (PM5 SUSS MicroTech) linked to a spectrum analyzer (VNA Agilent-N5) to generate the waves. We connect the first probe to the first set of IDTs to apply a sinusoidal voltage, while the second probe measures the resulting signal at the second set of IDTs. As we work with a delay-line configuration, we use the $S12$ parameter for electrical characterizations, representing the electrical power transferred from port 2 to port 1 [51–53]. The probe station is equipped with a temperature-controlled sample holder, and the measurements are conducted under a fixed temperature of 30 °C to limit the fluctuation of ambient temperature. The spectrum analyzer allows automatic signal processing by selecting a temporal range for the transmitted signal before Fourier transform to smoothen the response. We exclude from the temporal signals the periods that do not correspond to the acoustic waves, and the time range chosen for the experiments is between 320 ns and 4 μs to exclude electromagnetic noises and retain all the information associated with the first mode of the Love wave.

The frequency spectra of the device responses are plotted in Fig. 3(b) for two types of samples: without pillars (black curve) and with hardbaked pillars (red curves).

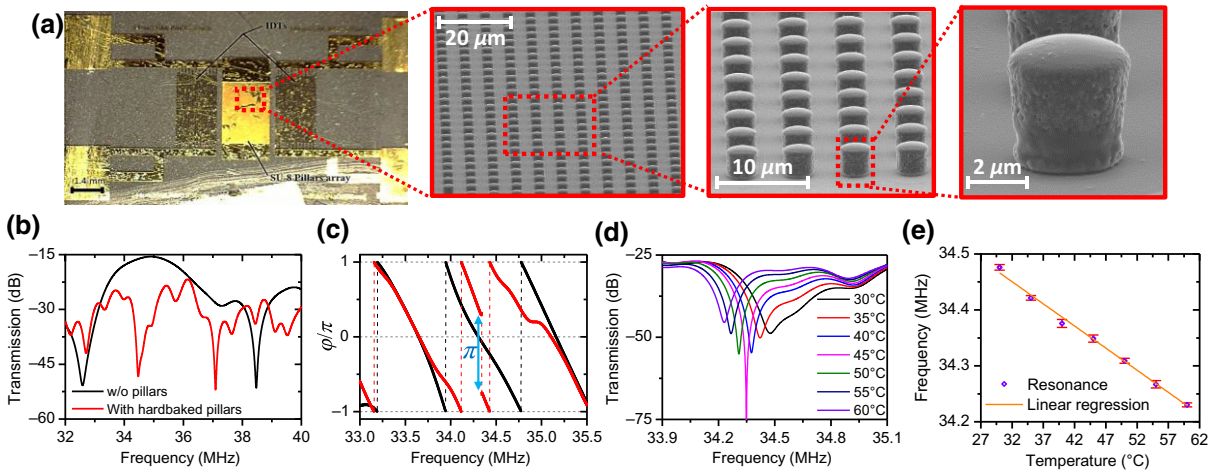

FIG. 3. (a) Images of the device recorded with a scanning electron microscope to show the array of pillars on different scales. (b) Experimental frequency spectrum of Love-wave transmission without pillars (black curve) and with hardbaked pillars (red curve). (c) Phase of transmitted signals as a function of the frequency for the sample without pillars (black curve) and with pillars (red curve). (d) Evolution of the resonance dip as a function of the temperature. (e) Linear dependency of the resonance frequency with temperature. The dots are measurements of the position of the dip with error bars, and the red line is the linear regression curve.

For the case without pillars (black curve), one can observe the central lobe associated with the excitation of the Love wave by the delay lines delimited by the dips of low transmission at 32.5 and 38.5 MHz.

For the sample with hardbaked pillars (red curves), an additional dip is depicted at the central lobe at 34.47 MHz, which is created by the excitation of the flexural vibration of the pillars. We also present in Fig. 3(c) the phase of the transmitted signal ($S21$ parameter) as a function of the frequency, where we can observe a phase jump of π at 34.47 MHz associated with the resonance of the pillars. Furthermore, the tendency of the measured resonance frequency closely corresponds to that found in the simulations. So, we can safely assume that the dip corresponds to the flexural resonance of the pillars. Additionally, we study the effect of the hardbaking process on the resonance dip by investigating the transmission signals for pillars with and without the hardbaking process, and the discussion is provided in Appendix B. Furthermore, we also experimentally study the effect of changing the pillars heights on their resonances (see Appendix C).

IV. SENSING EXPERIMENTS

The sensing performance of our device is tested for the detection of temperature variation, mass loading, sugar concentration, and polystyrene microbeads concentration. In these investigations, we use the hardbaked pillars, as they offer a high quality factor in the observed resonances (see Appendix B).

A. Temperature sensing

To observe the effect of temperature on the position of the resonance, we heat the substrate from 30 to 60 °C and measure the resonance frequency 9 times with a gradual increase and decrease in temperature. The measurements show that the resonance frequency of the pillars decreases with the increase in temperature [Fig. 3(d)]. The quality factor of the flexural resonance increases up to 45 °C then decreases. This effect can be explained by the common variation in the Young's modulus and the viscoelastic modulus of the hardbaked resin [54]. The frequencies reported during the increase and decrease in temperature overlap closely over the chosen range of temperature. Therefore, no hysteresis phenomenon will degrade the device after heating, which makes the device suitable for its utilization as a temperature sensor. The evolution of the resonance frequency shift with temperature is linear (coefficient of determination of $R^2 = 0.993$) with $\Delta f = 0.00795536\Delta T + 34.705$ MHz, which leads to a sensitivity of 229.23 ppm/K [Fig. 3(e)]. Table I provides a comparison between the sensitivity of our device and that of other SAW sensors in the literature providing high sensitivity for both Rayleigh- and Love-wave-based devices. Our device enables temperature sensing using Love waves with very high sensitivity.

B. Droplet-size sensing

To investigate the mass sensitivity of our device using the localized resonant mode of the pillars, we deposit microdroplets of distilled water on the pillar lattice using a micropipette. We acquire the signals for a set of droplet volumes from 2 to 7 μl, while maintaining a temperature of 30 °C [Fig. 4(a)]. Above 7 μl, the droplet size exceeds the pillars matrix surface, so it becomes irrelevant to increase the droplet size further. The device is dried between each measurement by increasing the temperature to 60 °C for

TABLE I. Comparison between the sensitivity of our device and that of existing studies.

	Type of wave	Substrate	Operating frequency (MHz)	Sensitivity (ppm/K)	Temperature range (°C)
Peng *et al.* [55]	Rayleigh	Langasite	226	105	68–73
Xu *et al.* [56]	Rayleigh	Langasite	408	167	−60 to 700
Ye *et al.* [57]	Rayleigh	$LiNbO_3$/YZ	437	79	0–80
Ye *et al.* [57]	Rayleigh	$LiNbO_3$/128°YX	497	66	0–80
Hu *et al.* [58]	Love	Polymethyl methacrylate on ST-cut quartz	...	0.75	25.6–27.6
Jakoby *et al.* [59]	Love	SiO_2 on AT-cut quartz	90; 115	50	30–45
Huang *et al.* [60]	Love	Carbon-fiber epoxy fiber on Mn:PIN-PMN-PT	...	126.6	25–55
This work	Love	SU8 on $LiNbO_3$	34.5	229.23	25–60

a few minutes until the water evaporates completely. The measurement results are shown in Fig. 4(b). We observe that the resonance frequency shifts towards low frequencies and the quality factor decreases with the volume of water added. This impact on the quality factor is due to the number of pillars covered by the droplet. Indeed, in addition to spreading the mass over a larger number of pillars, the viscosity of water will also impact more pillars. A greater number of pillars will disperse part of the wave energy into water, which is associated with a greater total energy loss and, therefore, a lower quality factor. Additionally, we observe that the resonance-frequency shift is linearly dependent on the volume of the droplet and, therefore, on the mass of deposited water.

C. Sugar-concentration sensing

To get closer to the experimental conditions of biodetection tests, we reproduce the same protocol as that in the previous section by fixing the droplet volume to 2.5 μl and using different solutions of sugar diluted in distilled water. The droplet is deposited on the pillars array, and a signal acquisition is performed. Between two measurements of solutions with different sugar concentrations, we rinse the sample with distilled water and dry it by heating it to 60 °C for a few minutes until all the water is evaporated. We test solutions with sugar concentrations from 0.1 to 20 mg/ml. The transmission curves around the resonance frequency of the pillars are shown in Fig. 4(c). We see that the frequency shifts toward lower frequencies as the concentration of sugar is increased. At the same time, we observe that the shape of the absorption dip changes. Its width decreases as the concentration increases, while the attenuation drops, resulting in an increase of the quality factor. This effect can be attributed to the variation of the viscosity with concentration. The viscosity of the solution is increasing from 0.89 mPa.s for the droplet of pure water (without sugar) to an estimated value of 1 mPa.s for the maximum concentration of 20 mg/ml [61–63]. We have, in this case, a combined influence of mass and viscosity on the resonance frequency that cannot be differentiated.

D. Sensing polystyrene microbeads in aqueous solution

To test the limit of detection of the system, we prepare several solutions of polystyrene microbeads with a mean diameter of 1 μm (Merck) to measure only the mass variation. The solutions have mass concentrations between 0.2 and 100 μg/ml. We use the same protocol for the measurements and rinsing of the device and repeat the measurements 11 times for each solution with a chosen concentration. The results of the frequency shift as a function of microbeads concentration are presented in Fig. 4(d). As previously, we observe that the frequency shifts towards lower frequencies with an increase of the concentration of the microbeads. Furthermore, unlike what is observed with sugar solutions, the shape of the dip is conserved at low concentrations (below 12.4 μg/l). In fact, we can observe that the shape of the dip changes drastically for concentrations higher than 12.4 μg/ml. In addition, the resonance frequency shifts to higher frequencies for concentrations higher than 25 μg/ml and becomes almost constant above 100 μg/ml. This effect is caused by the saturation in detection. Indeed, the density of polystyrene is close to that of the SU-8. For high concentrations, the apparent geometry of the resonators will be modified because of the deposition of microbeads on the pillars. Consequently, the apparent diameter of the pillars is increased, causing an increase of the resonance frequency. Figure 4(e) shows a linear evolution of the shift in frequency with the concentration of the microbeads in suspension in the droplets, up to 25 μg/ml. To calculate the sensitivity of our device, we first estimate the frequency change rate, $\Delta f/f_0$, where Δf is the frequency shift induced by a given concentration of microbeads, c_{NB}, within the microdroplet volume, V. As we fix this volume to $V = 2.5$ μl, the microdroplet covers an active surface of $\sigma = 5.12$ mm^2. The sensitivity can be

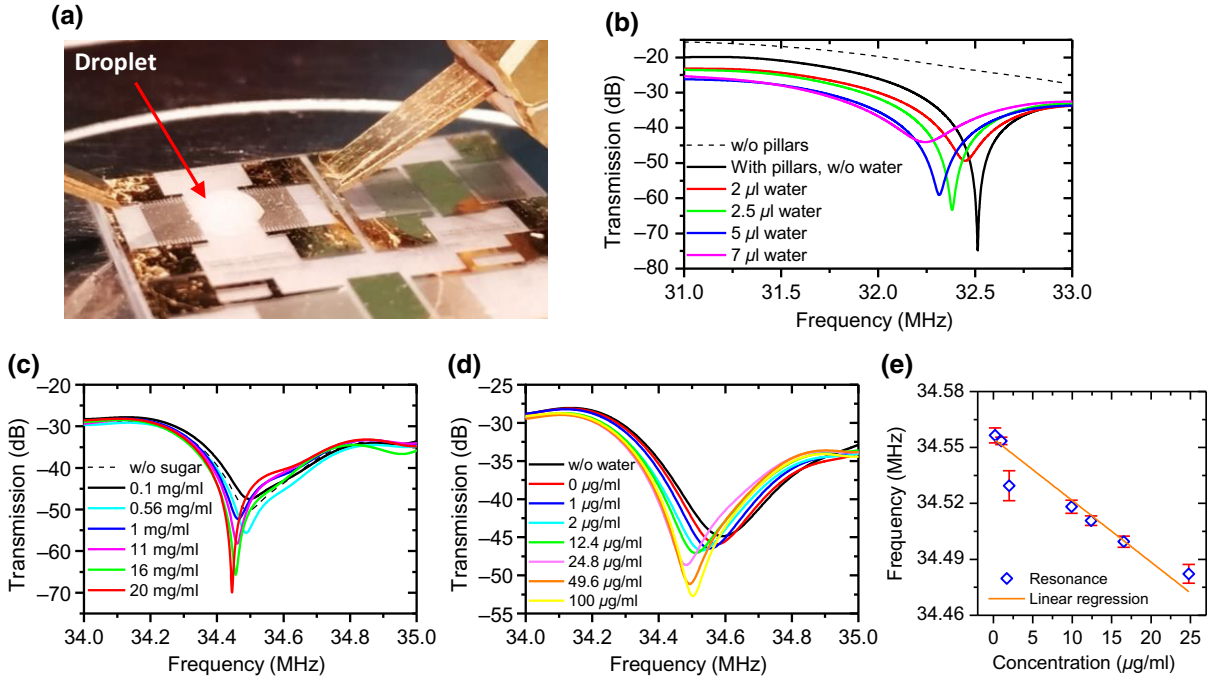

FIG. 4. (a) Image of the device with a droplet of microbeads solution deposited on top of the pillars array. Experimentally measured frequency shifts of the pillars resonances as a function of the volume of the droplet (b), the concentration of sugar in a microdroplet with a volume of 2.5 μl (c), and the concentration of polystyrene microbeads (d).

estimated by,

$$S = \left(\frac{\Delta f}{f_0}\right)\frac{\sigma}{c_{\mathrm{NB}}V}.$$

For a concentration of $c_{\mathrm{NB}} = 24.8$ μg/ml, we have a frequency shift of $\Delta f = 92.25$ kHz from the central frequency $f_0 = 34.5745$ MHz associated with a solution of pure water (zero concentration of microbeads). The sensitivity of our device is estimated to be 220.3 $\mathrm{m^2\ kg^{-1}}$. For the considered ratio of the guiding-layer thickness over the operating wavelength, $d/\lambda \approx 0.07$, this sensitivity value is 1 order of magnitude higher than that reported in the literature for Love-wave-based sensors using only IDTs [64].

V. CONCLUSION

Using a polymeric SU-8 photoresist, we fabricate an array of pillars on top of the guiding layer of a Love-wave-based sensor. The interaction between the Love waves and the natural resonances of the pillars produces sharp attenuations in the frequency spectra. By leveraging these resonances, we show that the sensor becomes more sensitive to temperature changes with a sensitivity of 7.96 kHz/°C. The sensor can also detect mass deposition of droplets on the pillars array. The device shows a linear evolution of the frequency shift with the mass deposition of polystyrene microbeads with a high sensitivity of 220.3 $\mathrm{m^2\ kg^{-1}}$ for concentrations below 25 μg/ml, which corresponds to 62.5 ng. This study offers experimental evidence of temperature and mass detections using localized resonances of the micropillars. These resonances are also affected by the viscosity of the liquid environment, so further investigations are to be conducted to separate the contributions of mass and viscosity. The present demonstration could open routes for future SAW-based sensing platforms with high sensitivity achieved by introducing and tailoring the pillars on the surface.

ACKNOWLEDGMENTS

The authors would like to thank the CNES (Centre National d'Etudes Spatiales) and the CNRS (Centre National de la Recherche Scientifique) for financial support.

APPENDIX A: BAND STRUCTURE

Figure 5 presents the acoustic band structure of the square lattice of pillars deposited on the surface of the SU8 guiding layer on the $LiNbO_3$ substrate. We indicate the sound line that separates the SAW from the bulk waves. As this type of SAW device supports both Rayleigh and Love waves, we focus only on Love waves by distinguishing the bands that have a dominant u_y displacement-component amplitude. This is done by evaluating the

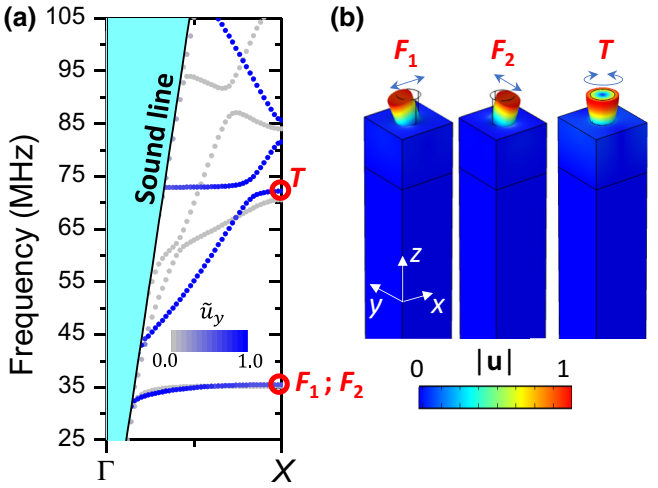

FIG. 5. Left panel, calculated band structure for the lattice of pillars on the SU-8/$LiNbO_3$ substrate. Gray-blue scale indicates the modes that have a dominant displacement component, u_y, amplitude in the direction perpendicular to the sagittal plane [Eq. (A1)]. Right, displacement fields of the resonant flexural and torsional modes at the X point of the Brillouin zone.

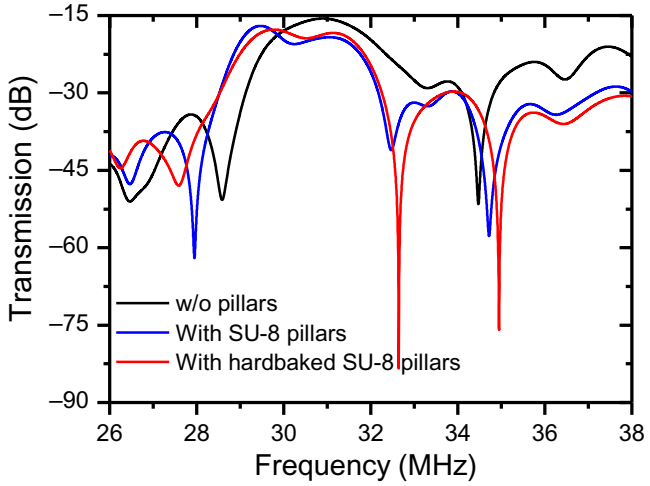

FIG. 6. Experimental frequency spectrum of the Love-wave transmission without pillars (black curve) and with SU-8 pillars without (blue curve) and with a hardbaking process (red curve).

following expression for each band [65]:

$$\tilde{u}_y = \frac{\int_V |u_y|^2}{\int_V |u_x|^2 + |u_y|^2 + |u_z|^2}, \tag{A1}$$

where the integral is taken over the volume of the guiding layer and the substrate in the considered unit cell.

The gray-blue color scale in the band structure indicates the modes with dominant u_y displacement-component amplitude. We can clearly distinguish the coupling between the Love-wave band and the resonance flexural mode F_2 at 35.4 MHz and torsional mode T at 72.2 MHz. The flexural resonance mode F_1 vibrates along the x direction, so it cannot be excited by Love waves.

APPENDIX B: COMPARISON BETWEEN NONHARDBAKED AND HARDBAKED PILLARS

The frequency-spectrum responses are plotted in Fig. 6 for three types of samples: without pillars (black curve), with pillars before hardbaking (blue curve), and with hardbaked pillars (red curve). The pillars here have an average height of 4.2 μm and an average radius of 3.5 μm. The shape of the signals remains globally the same for the three samples, but one can observe that an attenuation dip appears for the case of samples with pillars around a frequency of 32.5 MHz. These dips are associated with the excitation of the flexural vibration of the pillars. For the case of nonhardbaked (NHB) pillars (blue curve), the dip is located at 32.47 MHz with an attenuation of 20 dB. The quality factor for this resonance is estimated to be $Q_{\mathrm{NHB}} = 120$. Meanwhile, the frequency spectrum for the sample with hardbaked (HB) pillars (red curve) displays the dip at slightly higher frequency, 32.65 MHz, with a significant increase in the attenuation to 60 dB as well as for the quality factor, $Q_{\mathrm{HB}} = 510$. The shift of the resonance frequency to higher values by the hardbaking is expected because the dimensions of the pillars are reduced. In addition, since the guiding layer is hardbaked before the deposition of the pillars, there is an acoustic impedance mismatch between the guiding layer and the nonhardbaked pillars. This explains why the attenuation is higher in the case of the hardbaked pillars in comparison to the nonhardbaked-pillars case. The impedance match between the hardbaked pillars and the guiding layer favors the strain-energy transmission carried out by the wave into the pillars. This phenomenon is accompanied by an increase in the quality factor as well.

APPENDIX C: PILLARS RESONANCES AS A FUNCTION OF THEIR HEIGHTS

We study the effect of the pillars heights on the measured dip of the flexural resonance by comparing two samples with different pillars heights. The first sample, associated with the measurements in Fig. 3(b), has pillars with a height of 4 μm with a resonance frequency measured at 34.47 MHz, while the second sample presented in Fig. 6 has pillars with a height of 4.2 μm with the same radius and a measured resonance frequency of 32.5 MHz. In Fig. 7, we compare the numerical and measured resonance frequencies as a function of pillars height. We can clearly deduce that the increase in the pillars height shifts the resonance frequency to lower values with almost the same tendency in the experimental and numerical results. The slight difference between the theoretical results and the experimental ones is most likely due to the fact that

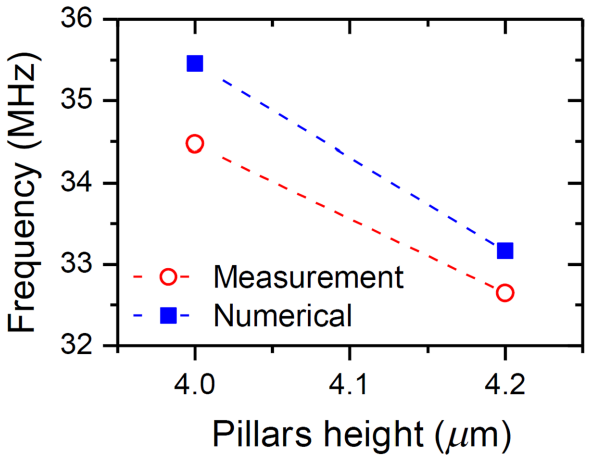

FIG. 7. Resonance frequency of the pillars as a function of pillar height and numerical (blue squares) and experimental measurements (red circles).

the fabricated pillars are not perfectly cylindrical in shape [see Fig. 3(a)].

[1] P. Mehrotra, Biosensors and their applications – a review, J. Oral Biol. Craniofacial Res. **6**, 153 (2016).

[2] V. Scognamiglio, F. Arduini, G. Palleschi, and G. Rea, Biosensing technology for sustainable food safety, TrAC Trends Anal. Chem. **62**, 1 (2014).

[3] K. Länge, B. E. Rapp, and M. Rapp, Surface acoustic wave biosensors: A review, Anal. Bioanal. Chem. **391**, 1509 (2008).

[4] J. Friend and L. Y. Yeo, Microscale acoustofluidics: microfluidics driven via acoustics and ultrasonics, Rev. Mod. Phys. **83**, 647 (2011).

[5] X. Ding, *et al.*, Surface acoustic wave microfluidics, Lab. Chip **13**, 3626 (2013).

[6] R. J. Shilton, M. Travagliati, F. Beltram, and M. Cecchini, Nanoliter-droplet acoustic streaming via ultra high frequency surface acoustic waves, Adv. Mater. **26**, 4941 (2014).

[7] S. Li, F. Ma, H. Bachman, C. E. Cameron, X. Zeng, and T. J. Huang, Acoustofluidic bacteria separation, J. Micromech. Microeng. **27**, 015031 (2016).

[8] F. Guo, *et al.*, Three-dimensional manipulation of single cells using surface acoustic waves, Proc. Natl. Acad. Sci. **113**, 1522 (2016).

[9] J. Qian, J. Ren, Y. Liu, R. H. W. Lam, and J. E.-Y. Lee, A two-chip acoustofluidic particle manipulation platform with a detachable and reusable surface acoustic wave device, Analyst **145**, 7752 (2020).

[10] Y. Huang, P. Kr. Das, and V. R. Bhethanabotla, Surface acoustic waves in biosensing applications, Sens. Actuators Rep. **3**, 100041 (2021).

[11] D. W. Branch and S. M. Brozik, Low-level detection of a bacillus anthracis simulant using Love-wave biosensors on 36°YX $LiTaO_3$, Biosens. Bioelectron. **19**, 849 (2004).

[12] W. Wang and S. He, Theoretical analysis on response mechanism of polymer-coated chemical sensor based Love wave in viscoelastic media, Sens. Actuators, B **138**, 432 (2009).

[13] Y. Zhang, F. Yang, Z. Sun, Y.-T. Li, and G.-J. Zhang, A surface acoustic wave biosensor synergizing DNA-mediated in situ silver nanoparticle growth for a highly specific and signal-amplified nucleic acid assay, Analyst **142**, 3468 (2017).

[14] C. Wu, A. B. Khanikaev, R. Adato, N. Arju, A. A. Yanik, H. Altug, and G. Shvets, Fano-resonant asymmetric metamaterials for ultrasensitive spectroscopy and identification of molecular monolayers, Nat. Mater. **11**, 69 (2012).

[15] K. V. Sreekanth, Y. Alapan, M. ElKabbash, E. Ilker, M. Hinczewski, U. A. Gurkan, A. De Luca, and G. Strangi, Extreme sensitivity biosensing platform based on hyperbolic metamaterials, Nat. Mater. **15**, 621 (2016).

[16] V. G. Kravets, A. V. Kabashin, W. L. Barnes, and A. N. Grigorenko, Plasmonic surface lattice resonances: A review of properties and applications, Chem. Rev. **118**, 5912 (2018).

[17] W. Yu, W. C. Jiang, Q. Lin, and T. Lu, Cavity optomechanical spring sensing of single molecules, Nat. Commun. **7**, 12311 (2016).

[18] Y. Zhi, X.-C. Yu, Q. Gong, L. Yang, and Y.-F. Xiao, Single nanoparticle detection using optical microcavities, Adv. Mater. **29**, 1604920 (2017).

[19] K. D. Heylman, N. Thakkar, E. H. Horak, S. C. Quillin, C. Cherqui, K. A. Knapper, D. J. Masiello, and R. H. Goldsmith, Optical microresonators as single-particle absorption spectrometers, Nat. Photonics **10**, 788 (2016).

[20] M. S. Kushwaha, P. Halevi, L. Dobrzynski, and B. Djafari-Rouhani, Acoustic band structure of periodic elastic composites, Phys. Rev. Lett. **71**, 2022 (1993).

[21] A. Khelif, M. Wilm, V. Laude, S. Ballandras, and B. Djafari-Rouhani, Guided elastic waves along a rod defect of a two-dimensional phononic crystal, Phys. Rev. E **69**, 067601 (2004).

[22] S. Yang, J. H. Page, Z. Liu, M. L. Cowan, C. T. Chan, and P. Sheng, Focusing of Sound in a 3D Phononic Crystal, Phys. Rev. Lett. **93**, 024301 (2004).

[23] S. Benchabane, A. Khelif, J.-Y. Rauch, L. Robert, and V. Laude, Evidence for complete surface wave band gap in a piezoelectric phononic crystal, Phys. Rev. E **73**, 065601 (2006).

[24] S. Mohammadi, A. A. Eftekhar, A. Khelif, W. D. Hunt, and A. Adibi, Evidence of large high frequency complete phononic band gaps in silicon phononic crystal plates, Appl. Phys. Lett. **92**, 221905 (2008).

[25] M. Oudich, M. Senesi, M. B. Assouar, M. Ruzenne, J.-H. Sun, B. Vincent, Z. Hou, and T.-T. Wu, Experimental evidence of locally resonant sonic band gap in two-dimensional phononic stubbed plates, Phys. Rev. B **84**, 165136 (2011).

[26] A. Oseev, M. Zubtsov, and R. Lucklum, Gasoline properties determination with phononic crystal cavity sensor, Sens. Actuators, B **189**, 208 (2013).

[27] X. Zhou, M. B. Assouar, and M. Oudich, Acoustic superfocusing by solid phononic crystals, Appl. Phys. Lett. **105**, 233506 (2014).

[28] S. Amoudache, Y. Pennec, B. Djafari Rouhani, A. Khater, R. Lucklum, and R. Tigrine, Simultaneous sensing of light and sound velocities of fluids in a two-dimensional PhoXonic crystal with defects, J. Appl. Phys. **115**, 134503 (2014).

[29] S. Benchabane, R. Salut, O. Gaiffe, V. Soumann, M. Addouche, V. Laude, and A. Khelif, Surface-Wave Coupling to Single Phononic Subwavelength Resonators, Phys. Rev. Appl. **8**, 034016 (2017).

[30] M. Badreddine Assouar and M. Oudich, Dispersion curves of surface acoustic waves in a two-dimensional phononic crystal, Appl. Phys. Lett. **99**, 123505 (2011).

[31] A. Khelif, Y. Achaoui, S. Benchabane, V. Laude, and B. Aoubiza, Locally resonant surface acoustic wave band gaps in a two-dimensional phononic crystal of pillars on a surface, Phys. Rev. B **81**, 214303 (2010).

[32] M. Oudich, B. Djafari-Rouhani, B. Bonello, Y. Pennec, S. Hemaidia, F. Sarry, and D. Beyssen, Rayleigh Waves in Phononic Crystal Made of Multilayered Pillars: Confined Modes, Fano Resonances, and Acoustically Induced Transparency, Phys. Rev. Appl. **9**, 034013 (2018).

[33] J. Bonhomme, M. Oudich, B. Djafari-Rouhani, F. Sarry, Y. Pennec, B. Bonello, D. Beyssen, and P. G. Charette, Love waves dispersion by phononic pillars for nano-particle mass sensing, Appl. Phys. Lett. **114**, 013501 (2019).

[34] L. Raguin, O. Gaiffe, R. Salut, J.-M. Cote, V. Soumann, V. Laude, A. Khelif, and S. Benchabane, Dipole states and coherent interaction in surface-acoustic-wave coupled phononic resonators, Nat. Commun. **10**, 4583 (2019).

[35] R. Lucklum and J. Li, Phononic crystals for liquid sensor applications, Meas. Sci. Technol. **20**, 124014 (2009).

[36] R. Lucklum, M. Ke, and M. Zubtsov, Two-dimensional phononic crystal sensor based on a cavity mode, Sens. Actuators, B **171–172**, 271 (2012).

[37] M. Zubtsov, R. Lucklum, M. Ke, A. Oseev, R. Grundmann, B. Henning, and U. Hempel, 2D phononic crystal sensor with normal incidence of sound, Sens. Actuators, A **186**, 118 (2012).

[38] A. Salman, O. A. Kaya, A. Cicek, and B. Ulug, Low-concentration liquid sensing by an acoustic Mach–Zehnder interferometer in a two-dimensional phononic crystal, J. Phys. Appl. Phys. **48**, 255301 (2015).

[39] S. Amoudache, R. Moiseyenko, Y. Pennec, B. D. Rouhani, A. Khater, R. Lucklum, and R. Tigrine, Optical and acoustic sensing using Fano-like resonances in dual phononic and photonic crystal plate, J. Appl. Phys. **119**, 114502 (2016).

[40] D. Nardi, E. Zagato, G. Ferrini, C. Giannetti, and F. Banfi, Design of a surface acoustic wave mass sensor in the 100 GHz range, Appl. Phys. Lett. **100**, 253106 (2012).

[41] J.-F. Robillard, A. Devos, and I. Roch-Jeune, Time-resolved vibrations of two-dimensional hypersonic phononic crystals, Phys. Rev. B **76**, 092301 (2007).

[42] Y. Achaoui, A. Khelif, S. Benchabane, L. Robert, and V. Laude, Experimental observation of locally-resonant and Bragg band gaps for surface guided waves in a phononic crystal of pillars, Phys. Rev. B **83**, 104201 (2011).

[43] D. Yudistira, A. Boes, B. Graczykowski, F. Alzina, L. Y. Yeo, C. M. Sotomayor Torres, and A. Mitchell, Nanoscale pillar hypersonic surface phononic crystals, Phys. Rev. B **94**, 094304 (2016).

[44] Y. Jin, Y. Pennec, B. Bonello, H. Honarvar, L. Dobrzynski, B. Djafari-Rouhani, and M. I. Hussein, Physics of surface vibrational resonances: pillared phononic crystals, metamaterials, and metasurfaces, Rep. Prog. Phys. **84**, 086502 (2021).

[45] C. Giannetti, *et al.*, Thermomechanical behavior of surface acoustic waves in ordered arrays of nanodisks studied by near-infrared pump-probe diffraction experiments, Phys. Rev. B **76**, 125413 (2007).

[46] B. J. Ash, S. R. Worsfold, P. Vukusic, and G. R. Nash, A highly attenuating and frequency tailorable annular hole phononic crystal for surface acoustic waves, Nat. Commun. **8**, 174 (2017).

[47] M. Oudich, B. Djafari-Rouhani, B. Bonello, Y. Pennec, and F. Sarry, Phononic crystal made of multilayered ridges on a substrate for Rayleigh waves manipulation, Crystals **7**, 12 (2017).

[48] B. J. Briscoe, L. Fiori, and E. Pelillo, Nano-indentation of polymeric surfaces, J. Phys. D: Appl. Phys. **31**, 2395 (1998).

[49] K. Geng, F. Yang, T. Druffel, and E. A. Grulke, Nanoindentation behavior of ultrathin polymeric films, Polymer **46**, 11768 (2005).

[50] A. T. Al-Halhouli, I. Kampen, T. Krah, and S. Büttgenbach, Nanoindentation testing of SU-8 photoresist mechanical properties, Microelectron. Eng. **85**, 942 (2008).

[51] K. Kurokawa, Power waves and the scattering matrix, IEEE Trans. Microw. Theory Tech. **13**, 194 (1965).

[52] S. R. Mazumder and P. D. van der Puije, Two-signal method of measuring the large-signal S-parameters of transistors, IEEE Trans. Microw. Theory Tech. **26**, 417 (1978).

[53] D. M. Pozar, *Microwave Engineering*, 4th ed. (Wiley, 1998).

[54] S. Chung and S. Park, Effects of temperature on mechanical properties of SU-8 photoresist material, J. Mech. Sci. Technol. **27**, 2701 (2013).

[55] L. Li, B. Peng, Y. Wang, B. Wang, H. Huang, W. Zhang, J. Zhu, and L. Liao, A novel design method for SAW temperature sensor with monotonic and linear frequency-temperature behavior in wide temperature range, Sens. Actuators, A **307**, 111982 (2020).

[56] H. Xu, H. Jin, S. Dong, J. Chen, X. Song, W. Xuan, L. Shi, S. Huang, P. Zhang, and J. Luo, A Langasite surface acoustic wave wide-range temperature sensor with excellent linearity and high sensitivity, AIP Adv. **11**, 015143 (2021).

[57] X. Ye, Q. Wang, L. Fang, X. Wang, and B. Liang, in 2010 IEEE SENSORS (2010), pp. 585–588.

[58] Y. W. Hu, J. W. Xiang, and X. Y. Sun, Temperature compensation experiment of Love wave sensor, Adv. Mater. Res. **490–495**, 673 (2012).

[59] B. Jakoby, J. Bastemeijer, and M. J. Vellekoop, Temperature-compensated Love-wave sensors on quartz substrates, Sens. Actuators, A **82**, 83 (2000).

[60] N. Huang, E. Sun, R. Zhang, B. Yang, J. Liu, T. Lü, L. Han, and W. Cao, Temperature dependence of normalized

sensitivity of Love wave sensor of unidirectional carbon fiber epoxy composite on Mn-doped 0.24PIN-0.46PMN-0.30PT single crystal substrate, Appl. Sci. **10**, 23 (2020).

[61] T. Soesanto and M. C. Williams, Volumetric interpretation of viscosity for concentrated and dilute sugar solutions, J. Phys. Chem. **85**, 3338 (1981).

[62] J. Chirife and M. P. Buera, A simple model for predicting the viscosity of sugar and oligosaccharide solutions, J. Food Eng. **33**, 221 (1997).

[63] M. Migliori, D. Gabriele, R. Di Sanzo, B. de Cindio, and S. Correra, Viscosity of multicomponent solutions of simple and complex sugars in water, J. Chem. Eng. Data **52**, 1347 (2007).

[64] H. Wu, X. Xiong, H. Zu, J. H.-C. Wang, and Q.-M. Wang, Theoretical analysis of a Love wave biosensor in liquid with a viscoelastic wave guiding layer, J. Appl. Phys. **121**, 054501 (2017).

[65] M. Oudich, B. Djafari-Rouhani, Y. Pennec, M. B. Assouar, and B. Bonello, Negative effective mass density of acoustic metamaterial plate decorated with low frequency resonant pillars, J. Appl. Phys. **116**, 184504 (2014).